RSC Advances

ROYAL SOCIETY OF CHEMISTRY

www.rsc.org/advances

Light Trapping in Hematite-Coated Transparent Particles for Solar Fuel Generation

Davood Danaei, [a] † **Raheleh Saeidi** [a] † and **Ali Dabirian**[b] *

Received Xth XXXXXXXXXX 20XX, Accepted Xth XXXXXXXXX 20XX
First published on the web Xth XXXXXXXXXX 200X
DOI: 10.1039/b000000x

Hematite (α-Fe_2O_3), due to its abundance and low-cost, is an attractive compound for photoelectrochemical splitting of water to produce hydrogen. However one major obstacle for hematite to fulfill the target efficiencies comprises its significantly smaller minority carrier transport distance relative to its optical absorption depth in the visible part of optical spectrum. Here we combine host-guest and Mie resonance concepts to achieve significant optical absorption in extremely thin layers of hematite. We propose and theoretically evaluate transparent particles coated with an extremely thin hematite layer as building blocks of hematite photoanodes. By full-field optical simulations we found out that maximal optical absorption is achieved when the particle supports two to three Mie resonance modes above the hematite optical absorption edge. Optical absorption efficiencies integrated over air mass 1.5 global (AM1.5G) irradiance spectrum, $<\eta_{abs}>_{AM1.5}$, reach to more than 2 mA.cm^{-2} within 10 nm thick hematite shell of a particle with optimal dimensions and $<\eta_{abs}>_{AM1.5}$ comes close to 5 mA.cm^{-2} in a 25 nm thick hematite shell. Furthermore we evaluate the performance when the particles are part of an array or stacked atop each other. The concept introduced here can be useful for improving optical absorption in semiconductors with extremely short carrier transport distances.

1 Introduction

Achievement of more than 5% solar to hydrogen efficiency in a solar hydrogen production device comprising bismuth vanadate ($BiVO_4$) photoelectrochemical (PEC) device biased with a double junction thin film silicon solar cell [1,2] have illustrated the bright future for PEC cells in hydrogen production. Despite such a progress with $BiVO_4$ [1–5] and also with compounds such as Ta_3N_5 [6–8] and oxynitrides, [9–11] α-Fe_2O_3 or hematite is still the most attractive water oxidation semiconductor due to its earth-abundance and the optical absorption edge of about 620 nm. [12,13]

To achieve highly efficient hematite photoanodes a number of approaches have been pursued so far to bypass the short minority carrier transport distance of 10 nm in hematite [13]. Network of hematite nanowires, [14–16] host-guest approach, [17–19] mesoporous hematite layers, [20,21] plasmonic nanostructures, [22,23] and using a reflective back-contact [24] are among different approaches that have been pursued. In addition, several sophisticated light trapping approaches have been recently proposed for hematite in which Mie resonance and/or host-guest approach (es) are used. [17,25–29]

Here we propose a photoanode design in which we combine the host-guest approach with Mie resonant optical absorption. Host-guest approach is a method in which a thin layer of hematite is conformaly coated onto a nanostructured conductive framework or onto an appropriate semiconductor with a large surface area. Mie resonances provide strong light trapping due to resonance effect and they are identified by having a large portion of their energy density close to the particle center; something that is not ideal for hematite because only optical absorption in hematite thickness of 10 nm away from hematite/electrolyte (EL) interface contributes to the water splitting process. For this reason, the Mie resonators we propose here comprise a transparent (for instance anatase TiO_2) core with a thin Fe_2O_3 shell. Transparency of the core is essential in building stacks of these spherical particles because the energy of light will not be dissipated within the core and therefore it can reach the layers underneath. On resonance the incident light is trapped inside the particle, the photon circulates within the particle, and hence light interaction with hematite shell is enhanced. We optimize the dimensions of TiO_2 particles coated with extremely thin layers of hematite (TiO_2@hematite) to maximize the optical absorption within hematite. Furthermore we evaluate the absorption efficiency of TiO_2@hematite particles integrated over air mass 1.5 global (AM1.5G) irradiance spectrum. We explore and identify the parameter space giving maximal sunlight absorption within

† These Authors contributed equally to this work.
[a] *Department of Physics, Tarbiat Modares University, P.O.BOX.14115-175,Tehran, Iran*
[b] *Photovoltaics and Thin Film Electronics Laboratory, Ecole Polytechnique Fédérale de Lausanne (EPFL), Rue de la Maladiére 71, Neuchatel 2000, Switzerland. Fax:+41 (0)21 6954261; Tel: +41 (0)21 6954201; E-mail: ali.dabirian@epfl.ch*

the carrier collection volume of hematite, described by a shell of 10 nm distance from Fe_2O_3/EL interface. In addition, we evaluate optical absorption in stacks or in an array of these particles to take into account the effect of multilayer formation and particles packing.

2 Results and discussion

Figure 1 (a) shows a schematic of TiO_2@hematite particle studied in this work in which the carrier collection volume is distinguished from rest of hematite by dashed line. The entire volume, illustrated by light-red color and defined by a volume of 10 nm distance from hematite/EL interface, designates the volume from which the photogenerated electron-hole pairs can be extracted with nearly 100% efficiency. The optical absorption edge of anatase TiO_2 is about 3.2 eV[30] therefore it does not absorb the visible light and as for ultraviolet light, it is absorbed in the hematite shell before reaching TiO_2. Therefore we design the particles dimensions such that they support weakly localized or low quality factor (low-Q) Mie resonance modes in the visible part of optical spectrum so that their electric field profile has a large overlap with hematite shell.

The basic scheme of a photoanodes that can be built from these core-shell TiO_2@hematite particles is schematically depicted in Figure 1b. It comprises a standard transparent conductive oxide (TCO) layer; i.e. F:SnO_2 also called fluorinated tin oxide (FTO) coated on glass. Directly on top of FTO there is an ultrathin (about 2 to 3 nm-thick) layer of Nb_2O_5[31] that can be deposited by atomic layer deposition (ALD)[31,32] or chemical vapour deposition (CVD)[33,34]. A 10 nm-thick hematite layer deposited by ALD on the Nb_2O_5 layer has been reported to result in about 0.5 mA.cm^{-2} photocurrent density at 1.23 V_{RHE} under 1 sun illumination.[31] V_{RHE} defines the reversible hydrogen electrode potential. Such a photoanode can be coated by a monolayer or several layers of TiO_2@hematite particles studied in this work as shown in Figure 1 to boost the optical absorption while keeping the distance that minority carriers need to travel short.

From a practical point of view, there are well-established processes to produce TiO_2 spherical particles of controlled diameters[35] that are useful for the concept introduced here. Then hematite can be coated onto these particles by for instance fluidized-bed ALD processes.[36,37] The particles can be fixed onto the substrate by sintering processes that are common in synthesis of hematite photoanodes.[21]

We begin by modeling the interaction of light with isolated TiO_2@hematite particles. From electromagnetic theory of spheres[38], also known as Mie theory, we expect these spheres to support resonance modes at sub-wavelength and wavelength scale dimensions. These resonance modes lead to resonant optical antenna effects that significantly enhance the optical absorption.[39–42] These optical antenna effects also occur in non-spherical dielectric and semiconductor structures in which the modal properties are described in the framework of the recently established leaky mode resonance theory.[39,40,43]

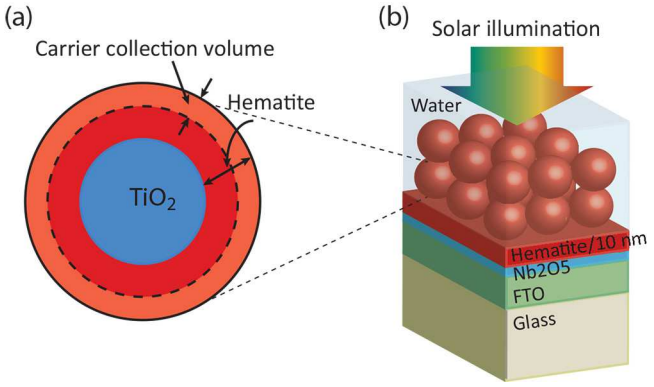

Fig. 1 (a) Schematic of the cross-section of a TiO_2@hematite particle in which the 10 nm carrier collection volume of hematite is illustrated. (b) Configuration of a hematite photoanode proposed in this work comprising a multilayer of resonant-size transparent (here TiO_2) particles coated with a thin shell of hematite. Such a configuration is proposed based on a successful extremely thin hematite device presented in the past.[31]

In spherical geometry the electromagnetic fields are expanded as the sum of spherical eigenmodes generally described as

$$\psi_{nml} = b_l(kr)p_l^m cos(\theta)\exp(\pm im\phi) \quad (1)$$

where $b_l(kr)$ is the spherical Bessel function and $P_l^m(cos\theta)$ is the associated Legendre function. Every spherical eigenmode is described by a set of (n,l,m) numbers where n is the number of field maxima inside the sphere in radial direction, l is the polar, and m is the azimuthal mode numbers. The number of anti-nodes in radial direction is described as n quantum number and it is obtained from the zeros of $b_l(kr)$. In polar direction, along θ-axis, the number of anti-nodes is obtained by $(m-l+1)$.[38,44]

In our calculations we model the sunlight as a plane wave described by $\vec{E}_{inc} = \vec{E}_0\exp(-i\vec{k}.\vec{r})$, where $\vec{k}$ is the wave-vector of the plane wave related to its frequency by $|k| = 2\pi f\sqrt{\varepsilon\mu}$ and $\vec{k}.\vec{r} = kx$ given the configuration of Figure 2a. The optical constants; i.e. refractive index and permittivity data, of Fe_2O_3 are acquired from the Literature.[45] Complex refractive index data of TiO_2 and Fe_2O_3 are reported in the Supplementary Information.

Interaction of this plane wave with isolated TiO_2@hematite particles in water is modeled at each wavelength of 300 nm to 620 nm range by numerically solving full-field Maxwell equations using the finite element method (FEM). We solve the equations for scattered fields using tetrahedral mesh and a perfectly matched layer (PML) boundary condition. The direct band gap of hematite is reported often between 1.9 to 2.2

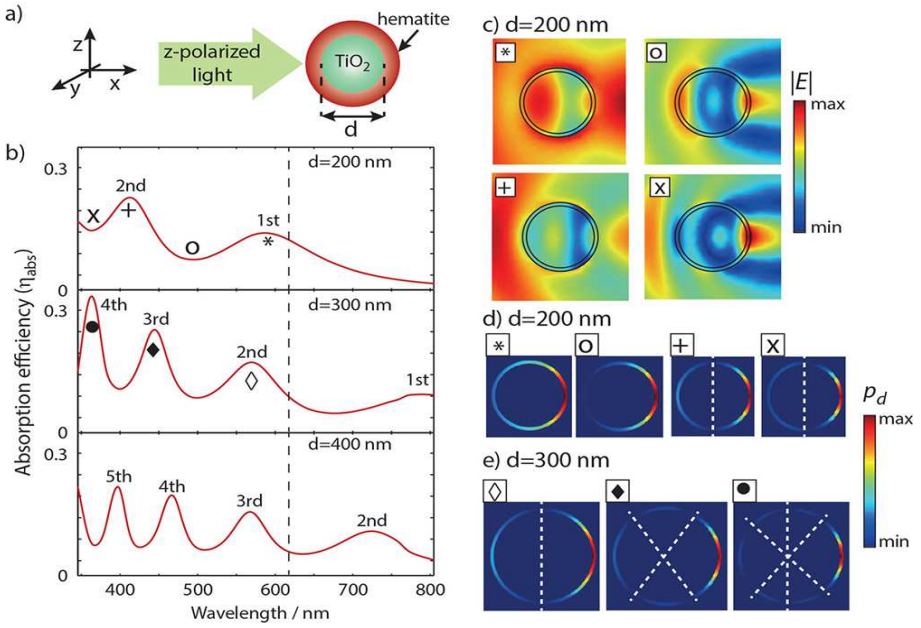

Fig. 2 a) Schematic of a TiO_2@hematite spherical particle under plane wave excitation in which the coordinate is defined. b) Absorption efficiency spectra for TiO_2@hematite particles with hematite shell of 10 nm and TiO_2 particle sizes of 200 nm, 300 nm, and 400 nm. Profile of (c) electric field amplitude and (d) dissipated power density in 200 nm TiO_2 particle with 10 nm hematite shell at four different wavelengths corresponding to the peaks and valleys of the absorption efficiency spectrum shown in part (b). e) Profile of dissipated power density ($P_d = \vec{E}.\vec{J}$) in 300 nm TiO_2 particles with 10 nm hematite shell at four different wavelengths corresponding to the peaks in the absorption efficiency spectrum shown in part (b).

eV[12] and here we consider 2 eV direct bandgap for hematite in our calculations. Electromagnetic fields calculated by FEM simulation are then used for calculating the absorption efficiency $\eta = C_{abs}/C_{geom}$ where C_{abs} is absorption cross-section and C_{geom} is geometrical cross-section of TiO_2@hematite particle.[46] C_{abs} is described by the ratio of absorbed power P_{abs} in the particle, $P_{abs} = \int \vec{J}(\vec{r},\lambda).\vec{E}(\vec{r},\lambda)d^3r$ to intensity of the incident light $I_{inc} = \frac{1}{2}\varepsilon c|E_{inc}|^2$. $\vec{J}(\vec{r},\lambda)$ describes the Ohmic electric current induced by electromagnetic waves in hematite shell and $P_d = \vec{J}(\vec{r},\lambda).\vec{E}(\vec{r},\lambda)$ describes the dissipated power density in $(\frac{W}{m^3})$.

Figure 2b shows the absorption efficiency spectra for TiO_2 particles of 200 nm, 300 nm, and 400 nm diameters coated with a 10 nm-thick hematite shell. In optical absorption efficiency spectrum of the 200 nm TiO_2 particle, two peaks are appeared that are labeled as zeroth (m=0) and first (m=1) order Mie resonance modes. At wavelengths shorter than 620 nm, i.e. the direct absorption edge of hematite, three and four peaks are observed in the absorption spectra of 300 nm and 400 nm TiO_2 particles, respectively. Comparison of these three spectra shows that i) the number of resonance peaks increases as particle size becomes larger and ii) the coupling of incident light to hematite shell is the largest for the 300 nm TiO_2 particles. The coupling extent is quantified by the amplitude of the absorption efficiency.

Profiles of electric field amplitude at peaks and valleys of the absorption efficiency spectrum of 200 nm TiO_2 particles are depicted in Figure 2c. At peaks wavelengths, the overlap of electric field with hematite shell is strong whereas at valleys this overlap is weak. This reconfirms the weak absorption in the valleys position because optical absorption is proportional to the intensity of electric field, i.e. electric field amplitude squared. This is more clearly illustrated in Figure 2d in which dissipated power densities (P_d=$\vec{E}.\vec{J}$) over the entire particle cross section are depicted.

We label the resonance modes based on the number of nodes in the profile of dissipated power density in hematite along azimuthal direction. For instance the zeroth Mie mode has no node within hematite shell whereas the first Mie mode has two nodes. Higher order Mie modes, i.e. second and third order modes, are excited in 300 nm TiO_2 particles with 10 nm hematite shell. Figure 2e shows the P_d profile in which the second (m=2) order mode is identified by four nodes and the third order (m=3) resonance modes by six nodes.

To evaluate the broadband optical absorption in TiO_2@hematite particles over the entire absorption band of hematite ($\lambda < 620$ nm) we calculate integrated weighted

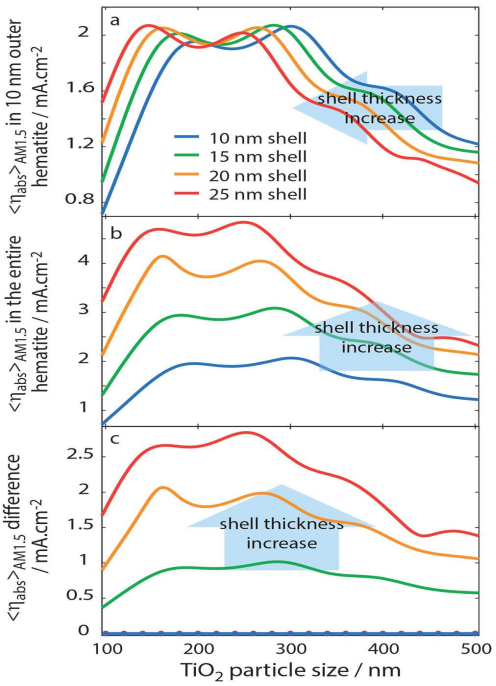

Fig. 3 Integrated AM1.5G weighted absorption efficiency (a) in the outer 10 nm hematite shell, (b) in the entire hematite, and (c) the difference of the two as size of TiO_2 particle varies from 100 nm to 500 nm at shell thicknesses of 10 nm, 15 nm, 20 nm, and 25 nm.

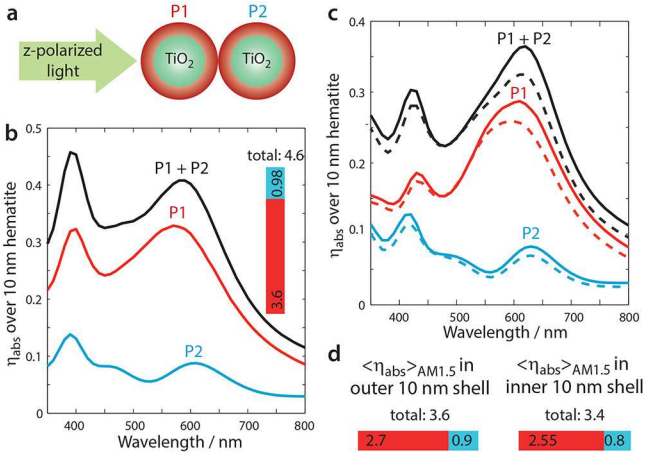

Fig. 4 (a) Schematic illustrating two stacked TiO_2@hematite particles illuminated by a plane-wave in which the particles exposed to the light first and second are designated as P1 and P2. (b) Absorption efficiency spectra of a stack of two 200 nm TiO_2 particles with 10 nm hematite shell. In the graph, contribution of optical absorption in each particle is specified. The bar in the inset shows $< \eta_{abs} >_{AM1.5}$ of the stack and also the contribution of each particle. (c) Absorption efficiency spectra of a stack of two 180 nm TiO_2 particles with 20 nm hematite shell. In the graph, contribution of optical absorption in each particle is specified; the solid line designate optical absorption in the 10 nm outer shell whereas the dashed line designate optical absorption within the 10 nm inner shell. (d) The bar on the left (right) shows $< \eta_{abs} >_{AM1.5}$ within the 10 nm outer (inner) hematite shells.

absorption efficiency described by[42,47–49]

$$< \eta_{abs} >_{AM1.5} = \frac{\int_{300}^{620} \eta_{abs}(\lambda).\phi_{AM1.5}(\lambda)d\lambda}{\int_{300}^{620} \phi_{AM1.5}(\lambda)d\lambda} \qquad (2)$$

where $\phi_{AM1.5}$ describes the irradiance spectrum of standard air mass AM1.5G illumination. $< \eta_{abs} >_{AM1.5}$ basically describes the ratio of the number of photons absorbed in hematite to the total number of above band gap photon flux passing through geometrical cross-section of the particle.

Figure 3a-c show calculated $< \eta_{abs} >_{AM1.5}$ in 10 nm outer hematite shell, in the entire hematite shell, and the difference of these two. Three peaks appear in $< \eta_{abs} >_{AM1.5}$ profile as TiO_2 particle size and hematite shell thickness vary from 100 nm to 500 nm and from 10 nm to 25 nm, respectively. The first peak corresponds to the case in which two Mie resonance exist in the 300 nm to 620 nm wavelength range. The second and the third peaks correspond to the cases in which three and four Mie resonance peaks exist in the wavelength range of interest for hematite.

$< \eta_{abs} >_{AM1.5}$ values in 10 nm outer hematite shell show maxima slightly larger than 2 mA.cm^{-2} for all hematite shell thicknesses as TiO_2 particle size varies. (Figure 3a) To determine the optimal thickness of hematite shell we need to minimize the portion of optical energy that is absorbed in part of the hematite that is not within the current collection volume because this energy is dissipated and it does not contribute to the water splitting process. Therefore we can conclude that given the 10 nm minority carrier transport distance in hematite, the 10 nm hematite shell is ideal. The energy loss becomes important when we make a multilayer of these TiO_2@hematite particles because in thicker hematite shells a large portion of optical energy is dissipated within the first few layers of these particles.(Figure 3c)

Figure 3b shows $< \eta_{abs} >_{AM1.5}$ in the entire hematite shell, revealing that the particles delivering maximal optical absorption have overall dimensions of 200 nm to 320 nm. In these dimensions two or three Mie resonance modes are excited in the particle in the 300 nm to 620 nm wavelength range. Total $< \eta_{abs} >_{AM1.5}$ reaches nearly 5 mA.cm $^{-2}$ in these conditions highlighting the efficient optical absorption in properly designed TiO_2@hematite particles. We should mention that such a high optical absorption becomes interesting if hole diffusion length of hematite could be extended to 25 nm, for instance using impurity doping.[50]

Stacks of several of these particles needs to be used to achieve larger photocurrent densities therefore to obtain an estimate of

how stacking influences the $< \eta_{abs} >_{AM1.5}$ values we study a stack of two TiO_2@hematite particles. We consider two optimal 220 nm TiO_2@hematite particles with 10 nm and 20 nm hematite shell thicknesses. Figure 4b shows the absorption efficiency of a stack of two 200 nm TiO_2 particles with 10 nm hematite shell along with absorption efficiencies of each sphere. The profile of absorption efficiencies for individual particles and also for the stack of two particles is somewhat different from absorption efficiency profile of a single particle shown in Figure 2b. This indicates that in two particles the scattered light from each particle interact with the other particle and therefore Mie resonance is not the only mechanism involved. The absorption efficiency of the first particle (P1) is significantly larger than absorption efficiency of a single particle (Figure 2b) whereas in the second one (P2) the absorption efficiency is smaller.

The $< \eta_{abs} >_{AM1.5}$ data were calculated for each particle and also for the stack of two particles and they are depicted as the bar chart shown in inset of Figure 4b. $< \eta_{abs} >_{AM1.5}$ in P1, P2 and the stack of two particles are 3.6, 0.98, and 4.6 $mA.cm^{-2}$ as shown in inset of Figure 4b. We should note that 4.6 $mA.cm^{-2}$ is produced in a hematite volume with nearly 100% carrier collection efficiency. Figure 4c shows absorption efficiencies of 10 nm inner/outer hematite shells for a stack of two 180 nm TiO_2 particles with 20 nm hematite shell along with the same data for each particle. It shows that a total of 7 $mA.cm^{-2}$ of AM1.5G light is absorbed in hematite out of which only 3.6 $mA.cm^{-2}$ is generated within 10 nm from hematite/EL interface. This is clearly smaller than 4.6 $mA.cm^{-2}$ that is generated in a stack two 200 nm TiO_2 particles with 10 nm hematite shell. In addition an equivalent of 3.4 $mA.cm^{-2}$ is dissipated in hematite, which cannot be recovered even if we use extra layers of the particles.

In an actual PEC device, an array or a stack of arrays of a large number of TiO_2@hematite particles is used. (Figure 1) Therefore we need to evaluate how the presence of adjacent particles influences optical absorption mechanism. Previous studies,[45,47] both theoretical and experimental, have shown that the results of isolated particles cannot be directly translated to large area devices composed of a large number of particles. This is due to two reasons: i) coupling among adjacent particles[47–49] and ii) presence of Fabry-Perot resonance modes in an ordered array of dielectric particles.[41,47,51]

To take the effect of adjacent particles into account we model interaction of a plane wave with 2 to 6 TiO_2(200 nm)@hematite(10 nm) particles packed in a hexagonal configuration with 10 nm spacing among each two particles, shown in inset of Figure 5a. Absorption efficiency was calculated by normalizing the absorption cross-section to area of a unit cell and it is depicted in Figure 5a. The unit cell is designated with a green hexagon in the inset of Figure 5a. Profile of absorption efficiency of these clusters of particles is no longer

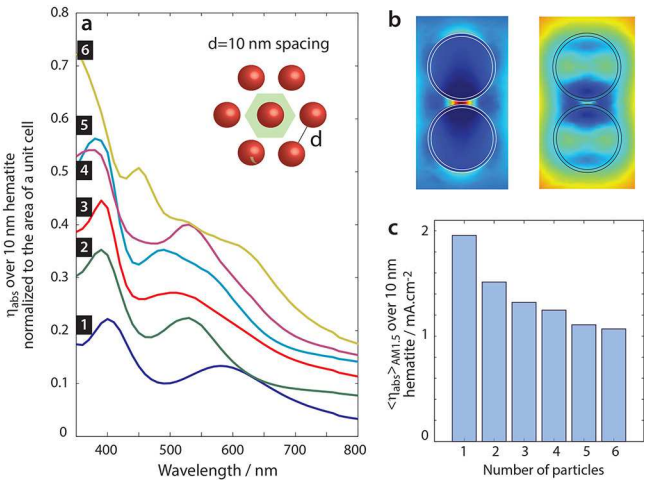

Fig. 5 (a) Optical absorption efficiency spectra of an array of one to six TiO_2 (200 nm)@hematite (10 nm) particles with 10 nm separation. Incident light impinges on the array from out of the plane. (b) The electric field profile at position of the peaks of absorption efficiency. (c) Integrated optical absorption efficiency normalized to the unit cell area for a hexagonal array of up to six of these TiO_2@hematite particles with 10 nm spacing.

the same as the one of a single particle. Several extra peaks appear in absorption efficiency, rising from coupling among adjacent particles. Electric field amplitude profile at the peaks of absorption efficiency for the case of 2 particles cluster does not show Mie resonance profile but it rises from the even and odd coupled modes of the particles. The profile in which the electric field is maximal between the two particles is similar to even (symmetric) mode and the other in which the electric field is rather stronger inside the particles comprise the odd (asymmetric) modal characteristic.

We further evaluate the influence of these adjacent particles on the overall AM1.5G integrated optical absorption by calculating $< \eta_{abs} >_{AM1.5}$ for the clusters of 2 to 6 particles with 10 nm interspacing between every two particles. Optical absorption was normalized to the total cross section of the cluster. Figure 5c shows the $< \eta_{abs} >_{AM1.5}$ and illustrate that due to presence of adjacent particles the overall absorption decays from about 2 $mA.cm^{-2}$ for a single particle to 1.15 $mA.cm^{-2}$ for a cluster of 6 particles. Extrapolating the data results in slightly more than 1 $mA.cm^{-2}$ for an infinite array of these particles. Therefore we expect a minimum of 1 $mA.cm^{-2}$ photocurrent for a monolayer of optimized 200 nm TiO_2 particles with 10 nm hematite shell.

3 Conclusion

Through full-field optical calculations, we have shown that transparent particles coated with an extremely thin layer of

hematite, if designed properly, efficiently absorb light within the 10 nm carrier transport distance of hematite. We found that the main critical design parameter is the overall size of the particle, which should be large enough so that the particle support two to three Mie resonance modes above the bandgap of hematite; i.e. the 300 nm to 620 nm wavelength range. In the stack of two particles, the performance scales linearly with the number of particles implying that a multilayer of these particles can be used for achieving maximal optimal absorption while keeping the distance that the minority carriers need to travel fixed. Presence of other particles in the vicinity of the particle deteriorates the optical absorption nearly to half. This is the situation that takes place when we build an actual PEC electrode from a large number of these particles. These particles can be synthesized using a combination of polyol and liquid-/gas-phase deposition methods and once synthesized, they can be applied to fabrication of large area devices using low-cost printing processes. Therefore the concept of transparent particles with a light-absorbing semiconductor shell can be applied for enhancing optical absorption in solar energy materials with short carrier transport distances.

4 Acknowledgement

The Authors thank Prof. A. Moshaii in Department of Physics, Tarbiat Modarres University for providing with computational facilities.

References

1 F. F. Abdi, L. Han, A. H. M. Smets, M. Zeman, B. Dam and R. van de Krol, *Nature Commun.*, 2013, **4**, 2195.

2 L. Han, F. F. Abdi, R. van de Krol, R. Liu, Z. Huang, H. Lewerenz, B. Dam, M. Zeman and A. Smets, *ChemSusChem.*, 2014, **7**, 2832-2838.

3 F. F. Abdi and R. van de Krol, *J. Phys. Chem. C* 2012, **116**, 9398.

4 F. F. Abdi, N. Firet, A. Dabirian and R. van de Krol, *MRS Proceedings* 2012, **1446**, mrss12-1446-u02-05, DOI :10.1557/opl.2012.811.

5 F. F. Abdi, A. Dabirian, B. Dam and R. van de Krol, *Phys. Chem. Chem. Phys.* 2014, **16**, 15272.

6 A. Dabirian and R. van de Krol, *Appl. Phys. Lett.*, 2013, **102**, 033905.

7 M. Higashi, K. Domen and R. Abe, *Energy Environ. Sci.*, 2011, **4**, 4138.

8 Y. Li, T. Takata, D. Cha, T. Minegishi, J. Kubota and K. Domen, *Adv. Mater.*, 2013, **25**, 125.

9 M. Higashi, K. Domen and R. Abe, *J. Am. Chem. Soc.*, 2012, **134**, 6968.

10 K. Maeda, M. Higashi, B. Siritanaratkul, R. Abe and K. Dome, *J. Am. Chem. Soc.*, 2011, **133**, 12334.

11 A. Dabirian, H. van't Spijker and R. van de Krol, *Energy Procedia*, 2012, **22**, 15.

12 J. H. Kennedy and K. W. Frese, *J. Chem. Sci*, 1978, **125**, 709-714.

13 K. Sivula, F. Le Formal and M. Grätzel, *ChemSusChem.*, 2011, **4**, 432.

14 J. Y. Kim, G. Magesh, D. H. Youn, J. Jang, J. Kubota, K. Domen and J. S. Lee, *Sci. Rep.*, 2013, **3**, 2684.

15 D. A. Wheeler, G. Wang, Y. Ling, Y. Li and J. Z Zhang, *Energy Environ. Sci.*, 2012, **5**, 6682.

16 Y. Ling, G. Wang, D. A. Wheeler, J. Z. Zhang and Y. Li, *Nano Lett.*, 2011, **11**, 2119.

17 Y. Qiu, S. Leung, Q. Zhang, B. Hua, Q. Lin, Z. Wei, K. Tsui, Y. Zhang, S. Yang and Z. Fan, *Nano Lett.*, 2014, **14**, 2123.

18 K. Sivula, F. L. Formal and M. Grätzel, *Chem. Mater.*, 2009, **21**, 2862.

19 Y. Lin, S. Zhou, S. W. Sheehan and D. Wang, *J. Am. Chem. Sco*, 2011, **133**, 2398.

20 S. D. Tilley, M. Cornuz, K. Sivula and M. Grätzel, *Angew. Chem. Int. Ed.*, 2010, **122**, 6549.

21 K. Sivula, R. Zboril, F. Le Formal, R, Robert, A. Weidenkaff, J. Tucek, J. Frydrych and M. Grätzel, *J. Am. Chem, Soc.*, 2010, **132**, 7436.

22 I. Thomann, B. A. Pinaud, Z. Chen, B. M. Clemens, T. F. Jaramillo and M. L. Brongersma, *Nano Lett.*, 2011, **11**, 3440.

23 M. Akbari, M.-R. Kikhavani, K. Sheshyekani and A. Dabirian, *RSC Adv.*, 2013, **3**, 17837.

24 H. Dotan, O. Kfir, E. Sharlin, O. Blank, M. Gross, I. Dumchin, G. Ankonina and A. Rothschild, *Nature Mater.*, 2013, **12**, 158.

25 K. X. Wang, Z. Yu, V. Liu, M. L. Brongersma, T. F. Jaramillo and S. Fan, *ACS Photonics.*, 2014, **1**, 235.

26 M. L. Brongersma, Y. Cui and S. Fan, *Nature Mater.*, 2014, **13**, 451.

27 S. J. Kim, I. Thomann, J. Park, J. Kang, A. P. Vasudev and M. L. Brongersma, *Nano Lett.*, 2014, **14**, 1446.

28 F. Boudoire, R. Toth, J. Heier, A. Braun and E. C. Constable, *Energy Environ. Sci.*, 2014, **7**, 2680.

29 S. Ramadurgam, T. Lin and C. Yang, *Nano Lett.*, 2014, **14**, 4517.

30 T. Tang, K. Prasad, R. Sanjines, P. E. Schmid and F. Levy, *J. Appl. Phys.*, 1994, **75**, 2042.

31 T. Hisatomi, H. Dotan, M. Stefik, K. Sivula, A. Rothschild, M. Grätzel and N. Mathews, *Adv. Mater.*, 2012, **24**, 2699.

32 S. M. George, *Chem. Rev.*, 2010, **110**, 111.

33 A. Dabirian, Y. Kuzminykh, E. Wagner, G. Benvenuti,

S. A. Rushworth and P. Hoffmann, *Chem. Phys. Chem.*, 2011, **12**, 3524.
34 A. Dabirian, Y. Kuzminykh, E. Wagner, G. Benvenuti, S. A. Rushworth and P. Hoffmann, *Thin Solid Films*, 2014 , **571**, 94.
35 X. Jiang, T. Herricks and Y. Xia, *Adv. Mater.*, 2003, **15** , 1205.
36 J. R. Scheffe, A. Francés , D. M. King, X. Liang, B. A. Branch, A. S. Cavanagh, S. M. George and A. M. Weimer, *Thin Solid Films*, 2009, **517** ,1874.
37 A. B. F. Martinson, M. J. DeVries, J. A. Libera, S. T. Christensen, J. T. Hupp, M. J. Pellin and J. W. Elam, *J. Phys. Chem. C*, 2011, **115**, 4333.
38 L. Tsang, J. A. Kong and K. Ding, John Wiley & Sons , 2004.
39 L. Cao, J. S. White, J. Park, J. A. Schuller, B. M. Clemens and M. L. Brongersma, *Nature Mater.*, 2009, **8** , 643.
40 L. Cao, P. Fan, A. P. Vasudev, J. S. White, Z. Yu, W. Cai, J. A. Schuller, S. Fan and M. L. Brongersma, *Nano Lett.*, 2010, **10**, 439.
41 S. Kim, R. W. Day, J. F. Cahoon, T. J. Kempa, K. Song, H. Park and C. M. Lieber, *Nano Lett.*, 2012, **12** , 4971.
42 S. A. Mann and E. C. Garnett, *Nano Lett.*, 2013, **13**, 3173.
43 Y. Yu, L. Cao, *Opt. Express*, 2012, **20** , 13847.
44 A. Dabirian and N. Taghavinia, *RSC Adv.*, 2013, **3** , 25417.
45 J. A. Glasscock, P. R. F. Barnes, I. C. Plumb, A. Bendavid and P. J. Martin, *Thin Solid Films*, 2008, **516** , 516, 1716.
46 C. F. Bohren, D. R. Huffman, John Wiley & Sons, 2008.
47 T. J. Kempa, R. W. Day, S. Kim, H. Park and C. M. Lieber, *Energy Environ. Sci.*, 2013, **6** , 719.
48 Y. Yu, V. E. Ferry, A. P. Alivisatos and L. Cao, *Nano Lett.*, 2012, **12** , 3674.
49 X. Zhang, C. W. Pinion, J. D. Christesen, C. J. Flynn, T. A. Celano and J. F. Cahoon, *J. Phys. Chem. Lett.*, 2013, **4** , 2002.
50 J. A. Glasscock, P. R. F. Barnes, I. C. Plumb and N. Savvides, *J. Phys. Chem. C.*, 2007, **11** , 16477.
51 A. Dabirian, *J. Opt.*, 2014, **16** , 075001.